

# Engineering Bound States in the Continuum at Telecom Wavelengths with Non-Bravais Lattices

Shunsuke Murai,\* Diego R. Abujetas, Libei Liu, Gabriel W. Castellanos, Vincenzo Giannini,\* José A. Sánchez-Gil,\* Katsuhisa Tanaka, and Jaime Gómez Rivas\*

Various optical phenomena can be induced in periodic arrays of nanoparticles by the radiative coupling of the local dipoles in each particle. Probably the most impressive example is bound states in the continuum (BICs), which are electromagnetic modes with a dispersion inside the light cone but infinite lifetime, that is, modes that cannot leak to the continuum.

Symmetry-protected BICs appear at highly symmetric points in the dispersion of periodic systems. Although the addition of nonequivalent lattice points in a unit cell is an easy and straightforward way of tuning the symmetry, BICs in such particle lattice, that is, non-Bravais lattice, are less explored among periodic systems. Starting from a periodic square lattice of Si nanodisks, three non-Bravais lattices are prepared by detuning size and position of the second disk in the unit cell. Diffraction-induced coupling excites magnetic/electric dipoles in each nanodisk, producing two surface lattice resonances at the  $\Gamma$  point with a band gap in between. The high/low energy branch becomes a BIC for the size/position-detuned array, respectively, while both branches are bright (or leaky) when both size and position are detuned simultaneously. The unexplored role of the interplay between magnetic and electric dipoles in dielectric nanoparticles in connection with the change of BIC to bright character in the detuned arrays is discussed with the aid of a coupled electric and magnetic dipole model. This study gives a simple way of tuning BICs at telecom wavelengths in non-Bravais lattices, including both plasmonic and dielectric systems, thus scalable to a wide range of frequencies.

particle can be radiatively coupled via in-plane diffraction, causing hybridized modes that are called surface lattice resonances (SLRs).<sup>[1–6]</sup> SLRs are characterized by narrow and strong resonances that appear in a wide spectrum range from terahertz<sup>[7]</sup> to ultraviolet,<sup>[8]</sup> depending on the periodicity of the lattice and the size of the particles. The arrays include 1D chains<sup>[9–11]</sup> and 2D lattices of particles. The most-studied 2D lattices are square and hexagonal patterns, which fall into two of the five Bravais lattices in 2D. In a Bravais lattice, all the particles are crystallographically equivalent and can be generated by a set of translation operations. Some works have explored non-Bravais lattices, where a second set of basis is introduced to the initial Bravais lattice.<sup>[12–21]</sup> This provides the nonequivalent lattice points in the unit cell, giving another channel for particle interaction. In many cases the second basis lowers the lattice symmetry, which changes the modes that can be excited in the system.

One related phenomenon that appears in periodic lattices is bound states in the continuum (BICs), which are bound (nonradiative or dark) eigenstates of an optical system despite having a dispersion within the light cone of the surrounding medium.<sup>[22–41]</sup> The quality ( $Q$ ) factor of a BIC approaches infinity in the absence of material losses, which is of particular interest

## 1. Introduction

Periodic arrays of resonant particles represent an arena of intensive research in modern optics. Localized resonances at each

S. Murai, L. Liu, K. Tanaka  
Department of Material Chemistry  
Graduate School of Engineering  
Kyoto University  
Nishikyo-ku, Kyoto 615-8510, Japan  
E-mail: murai@dipole7.kuic.kyoto-u.ac.jp

S. Murai, G. W. Castellanos, J. Gómez Rivas  
Department of Applied Physics and Eindhoven Hendrik Casimir Institute  
Eindhoven University of Technology  
P.O. Box 513, Eindhoven 5600 MB, The Netherlands  
E-mail: j.gomez.rivas@tue.nl

D. R. Abujetas  
Physics Department  
Fribourg University  
Chemin de Musée 3, Fribourg 1700, Switzerland

V. Giannini, J. A. Sánchez-Gil  
Instituto de Estructura de la Materia (IEM-CSIC)  
Consejo Superior de Investigaciones Científicas  
Serrano 121, Madrid 28006, Spain  
E-mail: v.giannini@csic.es j.sanchez@csic.es

V. Giannini  
Centre of Excellence ENSEMBLE3 sp. z o.o.  
Wolczynska 133, Warsaw 01-919, Poland  
V. Giannini  
Technology Innovation Institute  
Masdar City, Abu Dhabi 9639, United Arab Emirates

The ORCID identification number(s) for the author(s) of this article can be found under <https://doi.org/10.1002/lpor.202100661>

DOI: 10.1002/lpor.202100661

for lasing and sensing applications.<sup>[25,42–46]</sup> Symmetry-protected BICs often appear in high-symmetry points of the first Brillouin zone, such as at the  $\Gamma$  point. Defects and perturbations breaking the structural symmetries allow coupling of BICs to the radiative modes, transforming them into leaky resonances or quasi-BICs with a finite  $Q$ -factor.

Since the addition of a second basis lowers the lattice symmetry, non-Bravais lattices should represent a rich field for investigating and controlling BICs. BICs in a non-Bravais lattice have been recently reported in the terahertz (THz) and visible regions using metallic systems. In the THz region, a pair of gold resonant bars (dimer) sustain anti-parallel resonances that cancel each other, forming a BIC at the  $\Gamma$  point.<sup>[35]</sup> Such dimers have been also studied at optical frequencies, where pairs of silver nanoparticles in a lattice sustain a BIC mode.<sup>[12,13,16]</sup> Dielectric non-Bravais lattices have also been exploited.<sup>[32,47–49]</sup> Liu et al. achieved Huygens' metasurfaces based on zig-zag arrays of ellipsoidal Si nanoparticles supporting both electric and magnetic BICs via the interaction between pairs of in-plane electric or magnetic dipoles.<sup>[32]</sup> Vertchenko et al. explored directive BICs in near-zero index photonic crystals of Si hole arrays, where the detuning of hole radius reduces the lattice symmetry and limits the propagation direction of the BICs.<sup>[49]</sup> These works leave unexplored the interplay between in- and out-of-plane dipoles.

In this study, we unveil BICs emerging in non-Bravais rectangular lattices with different unit cell symmetries. The array consists of Si nanodisks which support both (in-plane and out-of-plane) electric and magnetic dipoles at telecom wavelengths. Therefore, the results presented here can be easily adaptable to any other dipolar lattice in contrast to metallic systems where only electric dipoles are excitable. We lower the symmetry of the initial square lattice by detuning the position and/or the size of the second nanodisk.<sup>[12,13,16,35]</sup> As we demonstrate in this manuscript, both operations induce a BIC emerging from different origins: the emergence of BICs is explained in an intuitive way based on the symmetry matching between the lattice and the magnetic and electric dipolar character of the mode, which is further verified by a theoretical model based on coupled electric and magnetic dipoles (CEMD).<sup>[50,51]</sup>

## 2. Non-Bravais Lattice with Size and Position Detunings

We design the non-Bravais lattices that support BICs in the telecom region starting from a square array of Si nanodisks. The array consists of polysilicon nanodisks arranged in a square lattice with a period of  $a_x = a_y = 425$  nm (see **Figure 1a**). This is the initial Bravais lattice structure that we call symmetric array. Note that the period is too short to sustain SLRs in the targeted telecom region. In the space group terminology, the symmetric array is classified as P4mm. Then we lower the symmetry of the lattice by shifting the position of the second disk by  $\delta x = 10\%$  from the original position (**Figure 1b**). The size of the unit cell is doubled by this operation ( $a_x = 850$  nm) and the second disk lies at  $2a_x/5 = 340$  nm away from the first disk. It is noted that the two disks in the unit cell are crystallographically not equivalent: that is, the lattice is non-Bravais. We call this array the position-detuned array (**Figure 1b**). The space group of the position-detuned array is Pmm2, where a mirror plane lies at the center of the unit cell

along the  $y$ -direction as indicated by a dotted line in the scanning electron microscopic (SEM) image. Another way of lowering the symmetry is to detune the size of the disk. The diameter of the second nanodisk is thus increased by  $\delta D = 32\%$  with respect to the first disk. This operation also makes  $a_x = 850$  nm and we call it the size-detuned array (**Figure 1c**). This array also falls into Pmm2 in space group, that is, the position- and size-detuned arrays have the same elements in terms of the symmetry. We also make a doubly-detuned array, where both the position and the size of the second disk are detuned from the first disk. The sample is called doubly-detuned array (**Figure 1d**). The space group of the doubly-detuned array is Pm; that is, the mirror planes along the  $y$ -direction are lost in this array. The detailed geometries of the arrays are found in **Table 1**.

## 3. Results and Discussion

### 3.1. Mode Dispersion at Telecom Frequencies

We measure the zeroth-order (forward) transmission spectrum by illuminating the sample with a collimated beam from a supercontinuum laser. To realize a homogeneous medium surrounding the nanodisks that provides out-of-plane symmetry, we place a quartz coverslip on top of the nanodisk array with refractive index matching oil ( $n = 2.1$ ) in between. We evaluate the optical extinction ( $E$ ), defined as  $E = 1 - T/T_0$ , where  $T$  is the transmission through the sample and  $T_0$  is the transmission through a reference consisting of a substrate, index-matching oil and superstrate. The extinction spectra are shown for TE-polarization in **Figure 1e–h** as a function of the angle of incidence,  $\theta_{in}$ , where the incident plane is defined in the  $z$ - $x$  plane.

For the symmetric array (**Figure 1e**), no extinction features appear in the range of measurement ( $\lambda$  between 1100 and 1500 nm) because the lattice resonances occur in the visible frequency range. On the other hand, for the position-detuned array (**Figure 1f**), highly dispersive features appear following the in-plane diffraction orders (Rayleigh anomalies), which correspond to the SLRs. The Rayleigh anomalies satisfy

$$\vec{k}_0 = \vec{k}_x(\theta_{in}) \pm \vec{G}(m_1, m_2) \quad (1)$$

where  $\vec{k}_0$  is the wave vector of the in-plane diffracted orders,  $\vec{k}_x$  is the in-plane component of the wave vector of the incident beam, and  $\vec{G}(m_1, m_2) = m_1(\frac{2\pi}{a_x})\vec{x} + m_2(\frac{2\pi}{a_y})\vec{y}$  is the reciprocal lattice vector of the array with  $m_1$  and  $m_2$  the orders of diffraction in the  $x$ - and  $y$ -directions, respectively. At the  $\Gamma$  point, the SLRs bend with a splitting energy of  $\approx 41$  meV between the upper and lower modes. The longer wavelength or lower-energy SLR becomes narrower as  $\theta_{in}$  approaches  $0^\circ$ , leading to a BIC at  $\theta_{in} = 0^\circ$  as seen in **Figure 1f**. SLRs also appear for the size-detuned array (**Figure 1g**), and interestingly enough, the BIC mode corresponds to the higher-energy SLR. For the doubly-detuned array (**Figure 1h**), both SLRs are bright. The cuts to the extinction dispersion measurements further show the evolution of the SLRs around the  $\Gamma$  point (**Figure 1i–l**).

The emergence of these BICs at the  $\Gamma$  point can be understood in an intuitive way upon considering the modes supported by the symmetric array and how they evolve as the symmetry of the lat-

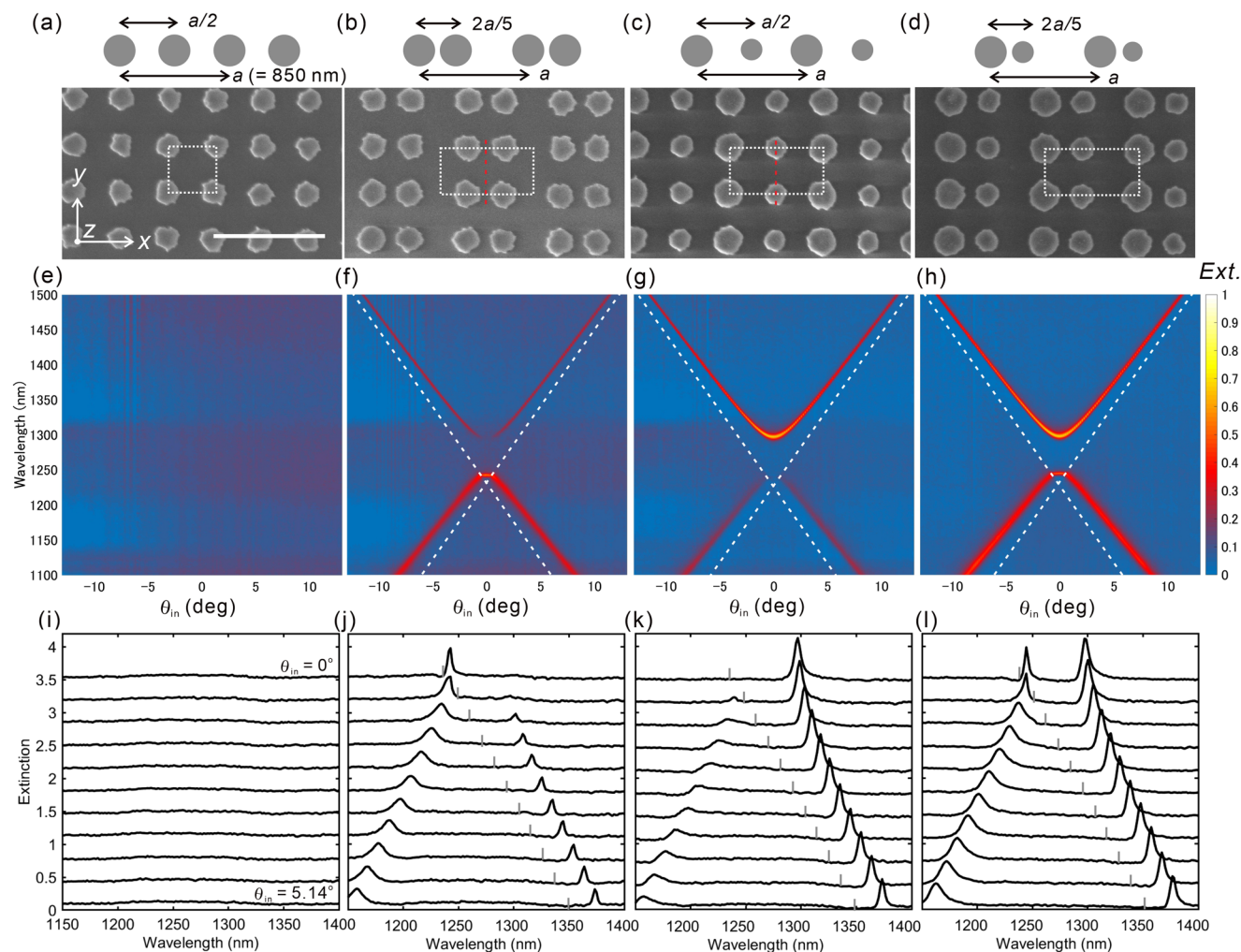


**Figure 1.** Structure and extinction of the nanodisk arrays. a–d) SEM images, e–h) extinction spectra for TE light as a function of angle of incidence  $\theta_{in}$  (in colormap), and (i–l) stacked spectra at  $\theta_{in}$  between 0 and 5.14° in steps of 0.514° : a,e,i) the symmetric, b,f,j) position-detuned, c,g,k) size-detuned and d),h),l) doubly-detuned array. In the SEM images, the scale bar is 1  $\mu\text{m}$  and the unit cell is denoted as white dashed boxes. The red lines indicate the mirror planes along the y-direction. The sketches of the disk arrangement along the x-direction are on the top. In the extinction spectra, the in-plane diffraction conditions are denoted as the dotted lines (colormap) and the vertical ticks (line spectra). The spectra were measured using a spectrometer with a resolution of 3.1 nm. The detailed geometries of the arrays are found in Table 1.

**Table 1.** The geometries of the four arrays: diameter of the first ( $D_1$ ) and second ( $D_2$ ) disk, the lattice constant in the x-direction ( $a_x$ ), and the center to center distance between the first and second disk. For  $D_1$  and  $D_2$ , both values experimentally obtained via SEM analysis and those used in CEMD calculation are listed. The disk height (200 nm) and the lattice constant in the y-direction ( $a_y = 425$  nm) are the same for all the arrays.

			Symmetric	Position-detuned	Size-detuned	Doubly-detuned
$D_1$	(exp.)	[nm]	$224 \pm 7.2$	$236 \pm 6.6$	$194 \pm 3.8$	$210 \pm 7.0$
$D_2$					$256 \pm 6.0$	$276 \pm 2.6$
$D_1$	(cal.)	[nm]	225	225	200	210
$D_2$					250	270
$a_x$		[nm]	850	850	850	850
Center-to-center distance		[nm]	$a_x/2$	$2a_x/5$	$a_x/2$	$2a_x/5$

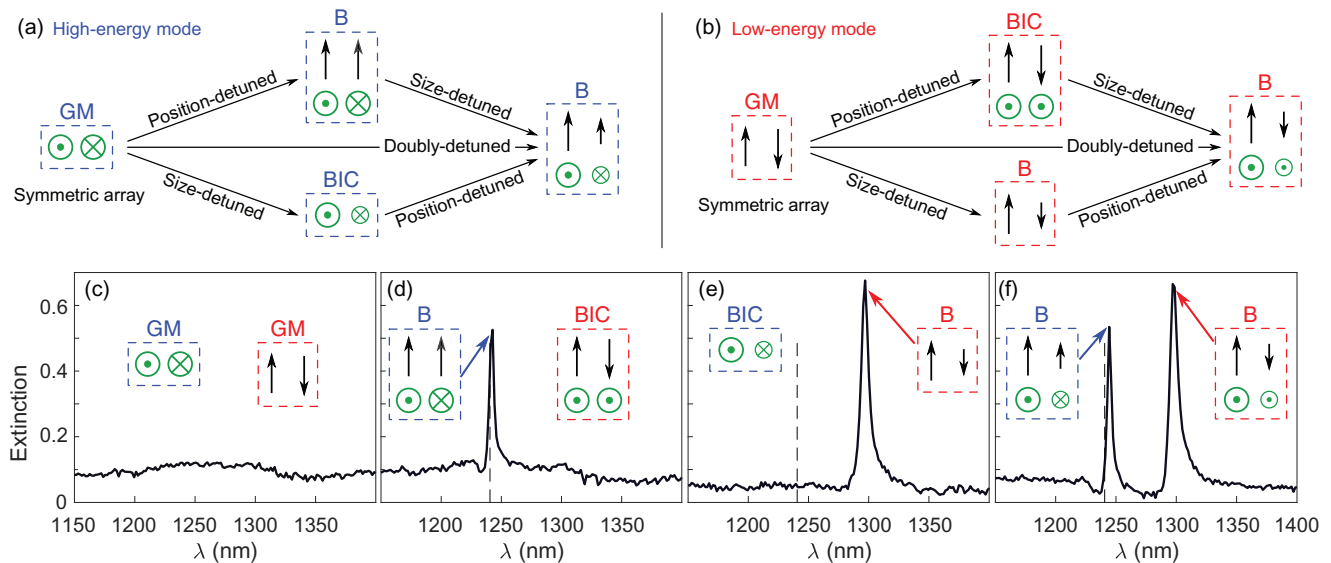


**Figure 2.** Schematic of mode evolution under lattice modification and correlation with extinction spectra (TE) at normal incidence ( $\theta_{in} = 0^\circ$ ). a) Evolution of the out-of-plane magnetic dipoles and b) of the in-plane electric dipoles eigenmodes from the guided modes in symmetric arrays to bright and BIC modes in other lattice symmetries. GM: guided mode, B: bright mode. c–f) Extinction spectra (TE) at normal incidence taken from Figure 1i–l. c) Symmetric, d) position-detuned, e) size-detuned, and f) double-detuned arrays. The insets show the eigenmodes supported by each lattice symmetry and the vertical dashed lines indicate the in-plane diffraction condition.

tice is changed, as depicted in **Figure 2a,b**. In the frequency range of interest, the symmetric array supports two guided modes given by the out-of-phase (anti-parallel) oscillation of in-plane electric dipoles ( $ED_y$ ) and out-of-plane magnetic dipoles ( $MD_z$ ). We will refer to them as the electric and magnetic guided modes, respectively. Since guided modes cannot be excited with propagating plane waves, the extinction spectrum shows no features (see Figure 1e,i). In contrast, for the other arrays, the perturbation of the unit cell doubles their size along the  $x$  axis and the dispersion relations of the guided modes fold down to the continuum of radiation. Therefore, the initially guided modes of the symmetric array evolve to leaky (bright) resonances or even to BICs.

For the position-detuned array, the displacement of the second disk in each (new) unit cell allows the coupling between  $ED_y$  and  $MD_z$ , forming hybrid modes. At the  $\Gamma$  point, the eigenstate stemming from the magnetic (electric) guided mode is given by anti-parallel oscillations of  $MD_z$  ( $ED_y$ ) mixed with parallel oscillations of  $ED_y$  ( $MD_z$ ), as depicted in Figure 2a(b). Note that both,  $ED_y$  and  $MD_z$ , oscillating parallel or anti-parallel are not self-consistent dipole configurations in the position-detuned array. Since the  $MD_z$  does not radiate in any case at the  $\Gamma$  point<sup>[52]</sup> and the anti-parallel  $ED_y$  cancels with each other, the electric guided mode evolves to a BIC (Figure 2b). In contrast, the magnetic guided mode evolves to a bright mode, due to the parallel oscillations of the  $ED_y$  associated to this eigenmode (Figure 2a). On the other hand, for the size-detuned array,  $ED_y$  and  $MD_z$  do not mix, but the relative strength between the dipoles in each cell is different. Therefore, the magnetic guided mode evolves to a BIC ( $MD_z$  does not radiate at the  $\Gamma$  point), while the electric guided mode evolves to a bright resonance, since the unequal amplitudes of the  $ED_y$  break the symmetry at normal incidence as seen in Figure 2a,b, respectively. Finally, for the doubly-detuned array, both resonances can couple to a plane wave at the  $\Gamma$  point, so that

both become bright. This is understood by combining the phenomenology exhibited for the position- and size-detuned arrays. The absence of symmetry-protected BICs is in accordance with the fact that the doubly-detuned array shows the lowest symmetry among the arrays in the present study.

The cuts to extinction spectra at normal incidence are shown in Figure 2c–f, together with the schematic of the modes supported by each lattice. The phenomenology described in terms of the eigenmodes of the systems adequately suits with the experimental results: The modes related to the magnetic guided mode are always at higher energies than those derived from the electric guided mode. Also, the mode frequency is only slightly altered upon a lattice perturbation (note that BIC frequencies can be estimated from the extinction dispersion spectra), suggesting that the framework depicted in Figure 2a,b is correct.

For the sake of completeness, the extinction for TM light is shown in Figure S1, Supporting Information. The two SLRs also appear for TM polarization, but the splitting is smaller ( $\approx 21$  meV). For this polarization, in-plane MDs instead of EDs couple to the diffraction order,<sup>[53]</sup> and a smaller splitting indicates a smaller in-plane magnetic polarizability of the Si nanodisk compared to the electric polarizability. For the position-detuned array, the BIC from anti-parallel  $MD_y$  mixed with parallel  $ED_z$  is supported, while anti-parallel  $ED_z$  creates the BIC for the size-detuned array.

### 3.2. CEMD Calculation

To confirm our intuitive explanation of the underlying physical mechanism, we have investigated theoretically the extinction of the arrays using a CEMD model.<sup>[51]</sup> We extract numerically the polarizability of electric and magnetic dipoles from the single



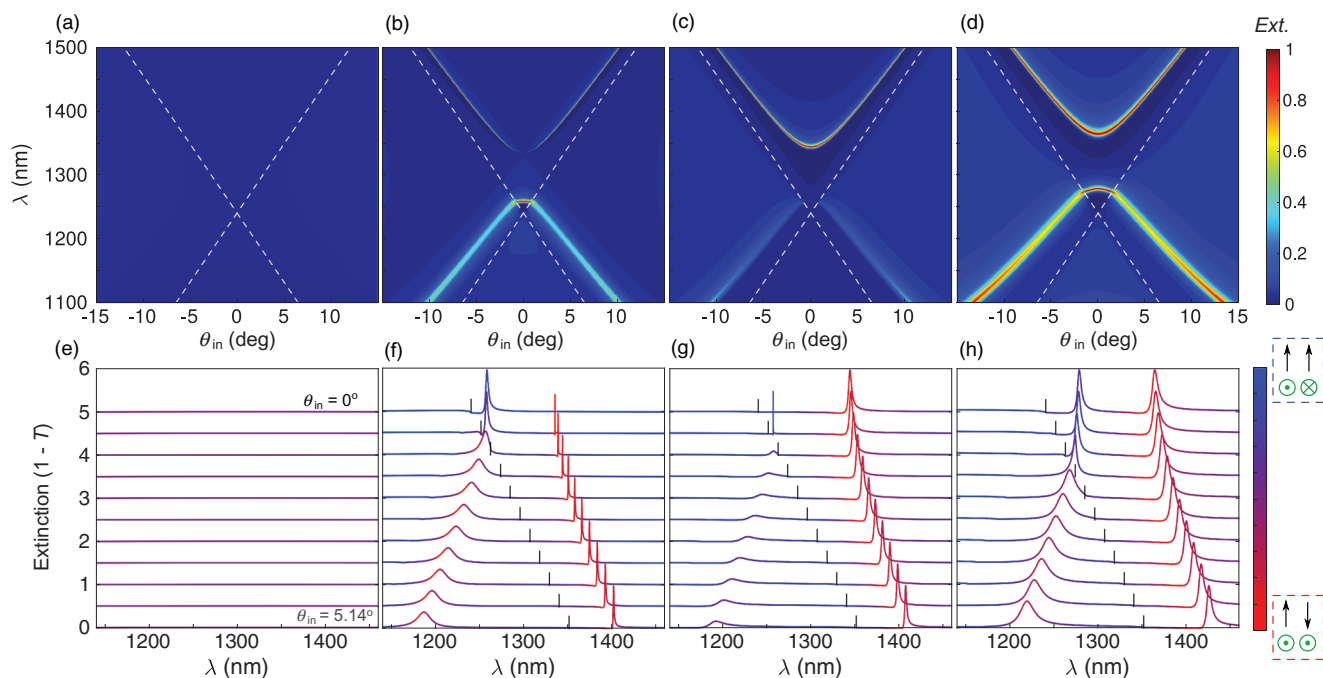


**Figure 3.** Extinction spectra of the nanodisk arrays calculated using the CEMD method for a) the symmetric, b) position-detuned, c) size-detuned, and d) doubly-detuned array. Upper panels show the extinction spectra (TE) as a function of  $\theta_{in}$ . e–h) The bottom panels are the spectra shown in a–d) between  $\theta_{in} = 0^\circ$  and  $5.14^\circ$  in steps of  $0.514^\circ$ . The color of the curves denotes the projection over the collective modes shown in the insets in Figure 2d–f): (red) low-energy mode with anti-parallel pairs of  $ED_y$  and parallel  $MD_z$ ; and (blue) high-energy mode with parallel  $ED_y$  and anti-parallel  $MD_z$ . The non-diffraction region is delimited by the vertical ticks.

disks, and calculate analytically  $1 - T$  (equivalent to the experimental extinction, since  $T$  is the specular transmittance) when the dipoles are arranged in an infinite lattice. The calculations shown in Figure 3a–d reproduce fairly well the experimental results in Figure 1e–h. No modes appear for the symmetric array as in the experiment. The flip of energy of the bright and BIC modes in position- and size-detuned arrays is clearly seen in Figure 3b,c, and the two bright modes at the  $\Gamma$  point are obvious for the doubly-detuned array (Figure 3d).

We further verify the intuitive assignment of the modes in Figure 2 by projecting the total calculated extinction into the in-plane and out-of-plane ED and MD components. The bottom panels in Figure 3 show the cuts to the extinction spectra around  $\theta_{in} = 0^\circ$ . The color of the lines for all three detuned arrays in Figure 3b–d reflects the origin of the modes, in accordance with the assignments in Figure 2 for the lower and higher energy bands: red represents the projection over the low-energy state with anti-parallel  $ED_y$  mixed with parallel  $MD_z$ , while blue denotes the projection over the high-energy state with anti-parallel  $MD_z$  mixed with parallel  $ED_y$ . This projection is done because these states are the theoretical eigenstates of the system at normal incidence. The brightness of the mode is determined by the position and magnitude of the dipoles, which are governed by the position and size of the disks, respectively, as explained in Figure 2. The projections of the theoretical results support the above-mentioned nature of the bands and the emergence of BICs at the  $\Gamma$  point in Figure 3f,g, only plausible with combinations of anti-parallel (identical) in-plane ED and/or arbitrary vertical MDs. Away from the  $\Gamma$  point the SLRs bands may exhibit more complex combi-

nations of dipolar states, as revealed in Figure 3f–h by the mixture of red/blue colors. We also plot separately the contributions from the  $ED_y$  and  $MD_z$  components to the total extinction as a function of frequency and angle of incidence in Figure S2, Supporting Information; note that the combination of both in-plane ED and out-of-plane MD contributions are needed to reproduce the discussed SLR bands and resulting BICs.

The direct evidence of the transition from quasi-BIC to symmetry-protected BIC is the resonance narrowing as it approaches  $\theta_{in} = 0^\circ$ . We extract the  $Q$ -factors from the two quasi-BICs appearing for the position- and size-detuned arrays in Figure 4. For the position-detuned array in Figure 4a, the  $Q$ -factor is so large that the value is above the resolution limit of the spectrometer (indicated by the dotted line in the plot) for all the measured angles. We also have plotted the  $Q$ -values extracted from the CEMD calculation by solid lines, showing a diverging behavior as  $\theta_{in}$  approaches  $0^\circ$ . For the size-detuned array (Figure 4b), the  $Q$ -factor increases as  $\theta_{in}$  approaches  $0^\circ$  and reaches the detection limit imposed by the resolution of the spectrometer. The agreement between the experiment and calculation is excellent. For the size-detuned array, we further analyzed the extinction with a spectrometer with a higher resolution and found that the  $Q$ -factor reached to 1600 (see Figure S3, Supporting Information for the extinction spectra). The diverging trend of the  $Q$ -value follows the calculation. This result might be surprising given the rough surface of the nanodisks as observed in the SEM images shown in Figure 1. One possible reason for the excellent agreement between experiments and calculations is the working wavelength in the present work: Telecom wavelengths are relatively

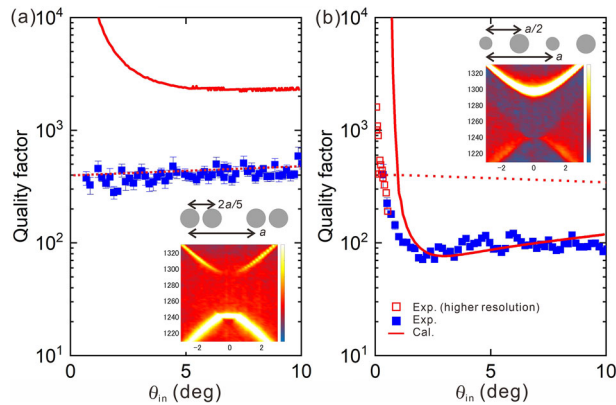


**Figure 4.**  $Q$ -factors of quasi-BIC mode extracted from the extinction in Figure 1 as a function of  $\theta_{in}$  for TE polarized light; a) the position-detuned array and b) the size-detuned array. The dotted lines indicate the upper limit of the  $Q$ -factor imposed by the resolution of the spectrometer. The open squares in b) is the  $Q$ -factor measured using a higher-resolution spectrometer (Q6370D Telecom Optical Spectrum Analyzer, Yokogawa, spectral resolution = 0.15 nm). See Figure S3, Supporting Information for the extinction spectra. The  $Q$ -factors extracted from the CEMD calculation in Figure 3 are shown as solid lines. The upper and lower insets are the schematic representation of the array and the optical extinction around normal incidence.

long compared to the surface imperfections and scattering can be neglected. Also the absorption of Si is negligible in this wavelength range, allowing the disks to be regarded as pure magnetic and electric dipoles.

### 3.3. Spectral Tuning of the BIC Position

In order to demonstrate the universality of the BICs appearing in rectangular non-Bravais lattice, we change the parameters in the design to shift the features. When the size of nanodisks is enlarged while the lattice constants remain the same, the two bands redshift with a larger splitting ( $\approx 83$  meV for TE light) due to the larger polarizability of the disks. Details are found in Section S4, Supporting Information.

We further shift the spectral features to the visible range by scaling the structure. The prepared size-detuned array consists of polysilicon nanodisks (86 and 107 nm diameters) arranged with  $a_x = 400$  nm and  $a_y = 200$  nm (see the inset in Figure 5c for the SEM image). The extinction shows a localized dispersionless band at  $\lambda \leq 500$  nm and the two SLRs (Figure 5). At  $\theta_{in} = 0^\circ$ , the high and low-energy bands appear with an energy gap of  $\approx 105$  meV for TE light (Figure 5a), and the higher-energy SLR becomes a BIC. For TM polarization (Figure 5b), the BIC mode

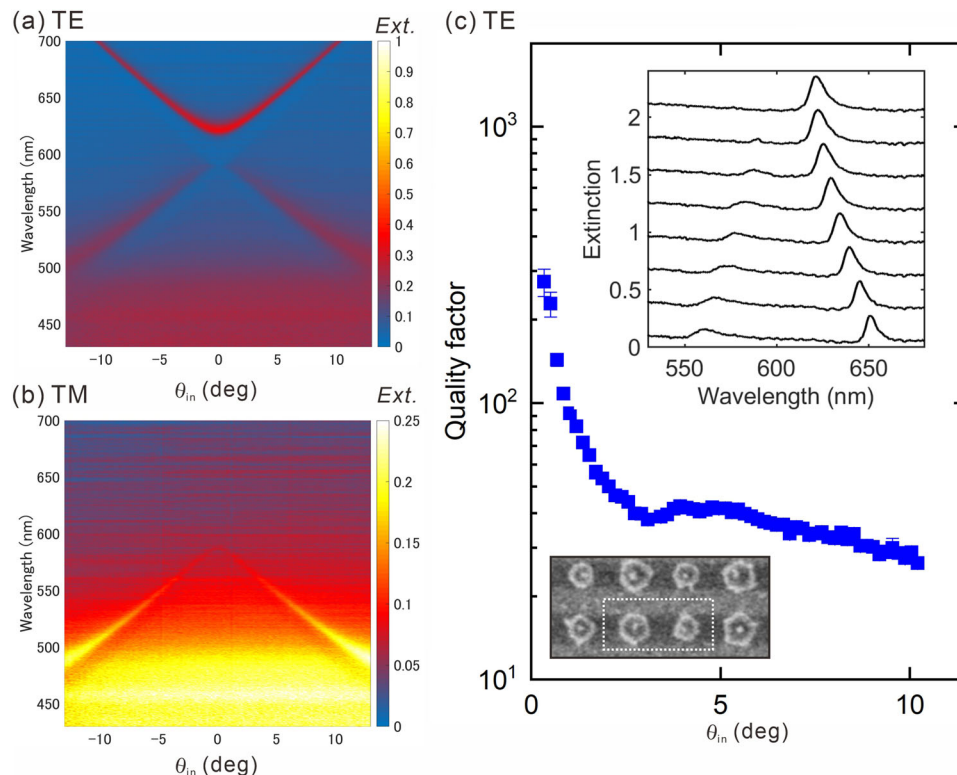


**Figure 5.** Optical properties of the size-detuned array resonating in the visible. The array consists of the pair of Si nanodisks (200 nm height, 86 and 107 nm diameters, center-to-center distance 200 nm) are arranged in the  $x$ - and  $y$ -directions with the period of 400 and 200 nm, respectively. a,b) Extinction spectra as a function of  $\theta_{in}$  for a) TE and b) TM polarized light. c)  $Q$ -factors of quasi-BIC mode extracted from the extinction as a function of  $\theta_{in}$  for TE-polarized light. The top inset is the extinction spectra around normal incidence ( $\theta_{in}$  between 0 to  $5.14^\circ$  every  $0.68^\circ$  step). The spectra are shifted vertically for the sake of clarity. The bottom inset is a top-view SEM image of the array. The dotted rectangle denotes the unit cell (400 nm  $\times$  200 nm) of the array.

is flipped to the lower energy band although less obvious due to a smaller magnetic polarizability. The appearance of BIC is evidenced by the  $Q$ -factor as a function of  $\theta_{\text{in}}$ , where  $Q$  diverges as  $\theta_{\text{in}}$  approaches  $0^\circ$  in Figure 5c.

## 4. Conclusions

We have demonstrated experimentally the emergence of symmetry-protected BICs at telecom wavelengths by detuning square arrays of polysilicon nanodisks into rectangular non-Bravais lattices. The initial square array supports two guided modes, comprising anti-parallel EDs and MDs, respectively, that turn into SLRs upon doubling the unit cell length in one direction by modifying the position/size of every other disk. Indeed, the interplay between EDs and MDs plays a crucial, unexplored role in the emergence of BICs, as follows. For the position-detuned array, the TE (TM) mode polarized along the short (long) axis of the lattice, consisting of horizontal anti-parallel EDs (MDs) mixes with vertical parallel MDs (EDs), becoming a BIC; for the size-detuned array, conversely, vertical anti-parallel MDs (EDs) lead to a BIC for the TE (TM) mode. When the symmetry of the lattice is further lowered by detuning size and position of the second nanodisks simultaneously, the symmetry-protected BICs disappear. The  $Q$ -factor of the quasi-BIC diverges as the incident angle approaches  $0^\circ$  and experimentally reaches 1600 for the size-detuned array. This work provides a robust design strategy of symmetry-protected BICs via introduction of a second meta-atom (nanodisk in this case) per unit cell to Bravais lattices, which is readily applicable to lasing, sensing, and light-matter coupling researches.

## 5. Experimental Section

**Fabrication:** Polycrystalline Si thin films with a thickness of 80 nm were grown on a synthetic silica glass substrate by low-pressure chemical vapor deposition using  $\text{SiH}_4$  gas as a source of Si. A resist (NEB22A2, Sumitomo) was cast on the Si film and exposed to electron-beam lithography, followed by development to make nanodisk arrays of resist on the Si film. The Si film was vertically etched using a selective dry etching (Bosch process) with  $\text{SF}_6$  and  $\text{C}_4\text{F}_8$  gases, and the resist residue was etched away by oxygen dry etching. The fabricated area of the array covers  $3 \times 3 \text{ mm}^2$ .

**Extinction Measurements:** The nanodisk arrays were in an optically homogeneous environment by placing an upperstrate of synthetic silica glass with index-matching oil. The samples were placed in a rotational stage, and illuminated by a collimated and polarized beam. The source of illumination was a broadband supercontinuum laser (FIANUM WHITELASE MICRO). The beam diameter was 0.1 mm, smaller than the area of the array. The optical axis corresponded to the z-axis and the sample was rotated around the y-axis (see Figure 1a). The polarization of the incident light was fixed either along the y-axis (TE polarization) or the x-axis (TM polarization). As the sample was rotated along the y-axis by an angle  $\theta_{\text{in}}$ , light was incident with a wave vector component that was parallel to the array plane along the x-direction,  $k_x = \frac{2\pi n}{\lambda} \sin \theta_{\text{in}}$ , where  $\lambda$  is the free-space wavelength and  $n$  is refractive index of the glass. The spectra was measured with a fiber-coupled spectrometer (NIR Quest, Ocean Optics) with 3.1 nm spectral resolution. The extinction was calculated as  $E = 1 - T/T_0$ , where  $T$  and  $T_0$  are the zeroth-order transmission measured on and off the array, respectively.

**CEMD Theoretical Calculations:** The coupled electric/magnetic dipole theory (CEMD) was used for infinite 2D planar arrays developed in refs. [50, 51]. In the case of disk meta-atoms with axes perpendicular to the metasurface, as explained in ref. [52], the polarizabilities of the in-plane

and out-of-plane, electric, and magnetic resonances were needed to apply the CEMD theory. These polarizabilities were numerically obtained through SCUFF,<sup>[54,55]</sup> an open-source software package for analysis of electromagnetic scattering problems using the method of moments, the dielectric function of polycrystalline silicon  $\epsilon = 3.5$ ,<sup>[56–58]</sup> and assuming a medium surrounding the nanodisks with  $\epsilon = 2.1$ . The four calculated polarizabilities were introduced in the CEMD model, that is, in- and out-of-plane MD and ED, which accounted for all lattice-induced interactions.

## Supporting Information

Supporting Information is available from the Wiley Online Library or from the author.

## Acknowledgements

This work was partly supported by the Nanotechnology Hub, Kyoto University (JPMXP09 F19NMC042) and Kitakyusyu FAIS in the “Nanotechnology Platform Project,” sponsored by MEXT, Japan. The authors gratefully acknowledge the financial support from Kakenhi (21H04619, 22H01776), JSPS Bilateral Program (JPJSBP120219920), and the Netherlands Organisation for Scientific Research (NWO) through Gravitation grant “Research Centre for Integrated Nanophotonics” and Innovative Research Activities Scheme (Vici project SCOPE no. 680-47-628). J.A.S.-G. and D.R.A. acknowledge support from the Spanish Ministerio de Ciencia e Innovación through grants MELODIA PGC2018-095777-B-C21 and FPU Ph.D. Fellowship FPU15/03566 (MCIU/AEI/FEDER, UE).

## Conflict of Interest

The authors declare no conflict of interest.

## Data Availability Statement

The data that support the findings of this study are available from the corresponding author upon reasonable request.

## Keywords

coupled electric, magnetic dipoles, silicon nanodisk arrays, surface lattice resonances

Received: November 19, 2021

Revised: July 11, 2022

Published online:

- [1] S. Zou, N. Janel, G. C. Schatz, *J. Chem. Phys.* **2004**, *120*, 10871.
- [2] Y. Z. Chu, E. Schonbrun, T. Yang, K. B. Crozier, *Appl. Phys. Lett.* **2008**, *93*, 181108.
- [3] V. G. Kravets, F. Schedin, A. N. Grigorenko, *Phys. Rev. Lett.* **2008**, *101*, 087403.
- [4] G. Vecchi, V. Giannini, J. Gómez Rivas, *Phys. Rev. Lett.* **2009**, *102*, 146807.
- [5] W. Zhou, T. W. Odom, *Nat. Nanotechnol.* **2011**, *6*, 423.
- [6] S. Collin, *Rep. Prog. Phys.* **2014**, *77*, 126402.
- [7] M. C. Schaafsma, A. Bhattacharya, J. G. Rivas, *ACS Photonics* **2016**, *3*, 1596.
- [8] Y. Kawachiya, S. Murai, M. Saito, H. Sakamoto, K. Fujita, K. Tanaka, *Opt. Express* **2018**, *26*, 5970.

- [9] S. Zou, G. C. Schatz, *Nanotechnology* **2006**, *17*, 2813.
- [10] E. M. Hicks, S. Zou, G. C. Schatz, K. G. Spears, R. P. Van Duyne, L. Gunnarsson, T. Rindzevicius, B. Kasemo, M. Käll, *Nano Lett.* **2005**, *5*, 1065.
- [11] S. R. Pockock, X. Xiao, P. A. Huidobro, V. Giannini, *ACS Photonics* **2018**, *5*, 2271.
- [12] A. D. Humphrey, N. Meinzer, T. A. Starkey, W. L. Barnes, *ACS Photonics* **2016**, *3*, 634.
- [13] A. Humphrey, W. Barnes, *J. Opt.* **2016**, *18*, 035005.
- [14] R. Guo, T. K. Hakala, P. Törmä, *Phys. Rev. B* **2017**, *95*, 155423.
- [15] Y. Hong, B. M. Reinhard, *Opt. Mater. Express* **2014**, *4*, 2409.
- [16] A. Cuartero-González, S. Sanders, L. Zundel, A. I. Fernández-Domínguez, A. Manjavacas, *ACS Nano* **2020**, *14*, 11876.
- [17] M. Esposito, F. Todisco, S. Bakhti, A. Passaseo, I. Tarantini, M. Cuscunà, N. Destouches, V. Tasco, *Nano Lett.* **2019**, *19*, 1922.
- [18] S. Baur, S. Sanders, A. Manjavacas, *ACS Nano* **2018**, *12*, 1618.
- [19] F. Todisco, M. Esposito, S. Panaro, M. De Giorgi, L. Dominici, D. Ballarini, A. I. Fernández-Domínguez, V. Tasco, M. Cuscunà, A. Passaseo, C. Ciraci, G. Gigli, D. Sanvitto, *ACS Nano* **2016**, *10*, 11360.
- [20] N. Mahi, G. Lévêque, O. Saison, J. Marae-Djouda, R. Caputo, A. Gontier, T. Maurer, P.-M. Adam, B. Bouhafs, A. Akjouj, *J. Phys. Chem. C* **2017**, *121*, 2388.
- [21] K. Guo, M. Du, C. I. Osorio, A. F. Koenderink, *Laser Photonics Rev.* **2017**, *11*, 1600235.
- [22] D. C. Marinica, A. G. Borisov, S. V. Shabanov, *Phys. Rev. Lett.* **2008**, *100*, 183902.
- [23] Y. Plotnik, O. Peleg, F. Dreisow, M. Heinrich, S. Nolte, A. Szameit, M. Segev, *Phys. Rev. Lett.* **2011**, *107*, 183901.
- [24] M. V. Rybin, K. L. Koshelev, Z. F. Sadrieva, K. B. Samusev, A. A. Bogdanov, M. F. Limonov, Y. S. Kivshar, *Phys. Rev. Lett.* **2017**, *119*, 243901.
- [25] C. W. Hsu, B. Zhen, A. D. Stone, J. D. Joannopoulos, M. Soljačić, *Nat. Rev. Mater.* **2016**, *1*, 16048.
- [26] S. Han, M. V. Rybin, P. Pitchappa, Y. K. Srivastava, Y. S. Kivshar, R. Singh, *Adv. Opt. Mater.* **2020**, *8*, 1900959.
- [27] K. Koshelev, G. Favraud, A. Bogdanov, Y. Kivshar, A. Fratalocchi, *Nanophotonics* **2019**, *8*, 725.
- [28] K. Fan, I. V. Shadrivov, W. J. Padilla, *Optica* **2019**, *6*, 169.
- [29] S. Kim, K.-H. Kim, J. F. Cahoon, *Phys. Rev. Lett.* **2019**, *122*, 187402.
- [30] K. Koshelev, S. Lepeshov, M. Liu, A. Bogdanov, Y. Kivshar, *Phys. Rev. Lett.* **2018**, *121*, 193903.
- [31] C. W. Hsu, B. Zhen, J. Lee, S.-L. Chua, S. G. Johnson, J. D. Joannopoulos, M. Soljačić, *Nature* **2013**, *499*, 188.
- [32] M. Liu, D.-Y. Choi, *Nano Lett.* **2018**, *18*, 8062.
- [33] J. W. Yoon, S. H. Song, R. Magnusson, *Sci. Rep.* **2015**, *5*, 18301.
- [34] N. Karl, P. P. Vabishchevich, S. Liu, M. B. Sinclair, G. A. Keeler, G. M. Peake, I. Brener, *Appl. Phys. Lett.* **2019**, *115*, 141103.
- [35] D. R. Abujetas, N. van Hoof, S. ter Huurne, J. Gómez Rivas, J. A. Sánchez-Gil, *Optica* **2019**, *6*, 996.
- [36] K. L. Koshelev, S. K. Sychev, Z. F. Sadrieva, A. A. Bogdanov, I. V. Iorsh, *Phys. Rev. B* **2018**, *98*, 161113.
- [37] T. G. Nguyen, G. Ren, S. Schoenhardt, M. Knoerzer, A. Boes, A. Mitchell, *Laser Photonics Rev.* **2019**, *13*, 1900035.
- [38] S. Han, L. Cong, Y. K. Srivastava, B. Qiang, M. V. Rybin, A. Kumar, R. Jain, W. X. Lim, V. G. Achanta, S. S. Prabhu, Q. J. Wang, Y. S. Kivshar, R. Singh, *Adv. Mater.* **2019**, *31*, 1901921.
- [39] Z. F. Sadrieva, I. S. Sinev, K. L. Koshelev, A. Samusev, I. V. Iorsh, O. Takayama, R. Malureanu, A. A. Bogdanov, A. V. Lavrinenko, *ACS Photonics* **2017**, *4*, 723.
- [40] J. F. Algorri, F. Dell'Olio, P. Roldán-Varona, L. Rodríguez-Cobo, J. M. López-Higuera, J. M. Sánchez-Pena, D. C. Zografopoulos, *Opt. Express* **2021**, *29*, 10374.
- [41] T. Yoda, M. Notomi, *Phys. Rev. Lett.* **2020**, *125*, 053902.
- [42] K. Hirose, Y. Liang, Y. Kurosaka, A. Watanabe, T. Sugiyama, S. Noda, *Nat. Photonics* **2014**, *8*, 406.
- [43] A. Kodigala, T. Lepetit, Q. Gu, B. Bahari, Y. Fainman, B. Kanté, *Nature* **2017**, *547*, 196.
- [44] S. T. Ha, Y. H. Fu, N. K. Emani, Z. Pan, R. M. Bakker, R. Paniagua-Domínguez, A. I. Kuznetsov, *Nat. Nanotechnol.* **2018**, *13*, 1042.
- [45] F. Yesilkoy, E. R. Arvelo, Y. Jahani, M. Liu, A. Tittl, V. Cevher, Y. Kivshar, H. Altug, *Nat. Photonics* **2019**, *13*, 390.
- [46] R. Heilmann, G. Salerno, J. Cuerda, T. K. Hakala, P. Törmä, *ACS Photonics* **2022**, *9*, 224.
- [47] V. V. Khardikov, E. O. Iarko, S. L. Prosvirnin, *J. Opt.* **2012**, *14*, 035103.
- [48] A. S. Kupriianov, Y. Xu, A. Sayanskiy, V. Dmitriev, Y. S. Kivshar, V. R. Tuz, *Phys. Rev. Appl.* **2019**, *12*, 014024.
- [49] L. Vertchenko, C. DeVault, R. Malureanu, E. Mazur, A. Lavrinenko, *Laser Photonics Rev.* **2021**, *15*, 2000559.
- [50] D. R. Abujetas, J. A. Sánchez-Gil, J. J. Sáenz, *Opt. Express* **2018**, *26*, 31523.
- [51] D. R. Abujetas, J. Olmos-Trigo, J. J. Sáenz, J. A. Sánchez-Gil, *Phys. Rev. B* **2020**, *102*, 125411.
- [52] S. Murai, D. R. Abujetas, G. W. Castellanos, J. A. Sánchez-Gil, F. Zhang, J. G. Rivas, *ACS Photonics* **2020**, *7*, 2204.
- [53] S. Murai, G. W. Gabriel, W. Castellanos, T. Raziman, A. G. Curto, J. Gómez Rivas, *Adv. Opt. Mater.* **2020**, *8*, 1902024.
- [54] M. H. Reid, S. G. Johnson, *arXiv:1307.2966* **2013**.
- [55] M. T. H. Reid, <http://homerreid.github.io/scuff-em-documentation/> (accessed: August 2022).
- [56] D. E. Aspnes, A. A. Studna, *Phys. Rev. B* **1983**, *27*, 985.
- [57] C. Schinke, P. C. Peest, J. Schmidt, R. Brendel, K. Bothe, M. R. Vogt, I. Kröger, S. Winter, A. Schirmacher, S. Lim, H. T. Nguyen, D. MacDonald, *AIP Adv.* **2015**, *5*, 067168.
- [58] M. A. Green, *Sol. Energy Mater. Sol. Cells* **2008**, *92*, 1305.